

# Multi-color Mock catalogues

S. Arnouts<sup>1</sup>, M.A.T. Groenewegen<sup>1</sup>, and L. da Costa<sup>1</sup>

<sup>1</sup> European Southern Observatory, Karl-Schwarzschild-Str. 2, D-85748 Garching b. München, Germany

<sup>2</sup> Observatoire de la Côte d’Azur, BP 229, 06304 Nice cedex 4, France

<sup>3</sup> Max-Planck Institut für Astrophysik, Karl-Schwarzschild-Str. 1, D-85748 Garching b. München, Germany

<sup>4</sup> Universidade Estadual de Feira de Santana, Campus Universitário, Feira de Santana, BA, Brazil

<sup>5</sup> Observatório Nacional, Rua Gen. José Cristino 77, Rio de Janeiro, R.J., Brasil

DRAFT VERSION: FEBRUARY 14, 2002

**Abstract.** We describe an empirical approach to generate multicolor-mock catalogues reflecting the observational conditions. Our method is applied to the specific cases of the Deep Public Survey carried out by EIS. In this paper, we investigate the impact of the choice of magnitudes in the results and the efficiency of the Deep Public Survey to select high- $z$  galaxies based on a color-color diagram. We also estimate the fraction of interlopers (low- $z$  galaxies and stars) in such selection box.

**Key words.** catalogs –surveys– galaxy – photometry –

## 1. Introduction

The successful application of photometric techniques to identify high-redshift galaxies ( $z \gtrsim 3$ ) combined with large-aperture telescopes with multi-object spectrographs have provided the means to study large-scale structures at high-redshifts and to directly probe their evolution over a broad range of redshifts. Currently, the challenge is to construct well-defined statistical galaxy samples at faint magnitudes and use color-selection or photometric redshift techniques to pre-select candidates for large spectroscopic surveys probing the high-redshift Universe. To achieve this goal, deep optical/infrared multi-passband surveys covering areas of the order of a few degrees are required. In this paper we generate mock catalogues to address some critical issues, relative to the efficiency of a survey characterised by their observational conditions, like the fraction of LBGs selected based on color-color diagram selection and the fraction of interlopers due to low- $z$  galaxies and stars.

## 2. Ingredients for building the simulated catalogues

The first ingredient of the simulations is the choice of the luminosity function per spectral type and its redshift evolution in a given passband. Each object at a given apparent magnitude and redshift is associated to a spectral energy distribution (SED) in order to derive its apparent magnitudes in different passbands. From this ideal realisation we associate to each object a luminosity profile which is combined to the observational conditions to derive different kind of realistic apparent magnitudes.

Send offprint requests to: Stephane Arnouts, e-mail: sarnouts@eso.org

The ingredients used in the simulations are described in this section. Throughout the paper, we adopt an Einstein-de Sitter universe ( $\Omega_0 = 1, \Omega_\Lambda = 0$ ) and  $H_0 = 50 h$  km/s/Mpc.

### 2.1. The Spectral Energy Distribution templates

To characterise the spectral properties of galaxies, we have used the Coleman-Extended (CE) list of SEDs as described in Arnouts et al. (1999) which have been shown to provide accurate photometric redshift estimates in the HDF fields. The CE list is based on the four observed spectra obtained by Coleman et al. (1980) corresponding to an Elliptical, Sbc, Scd and Irregular, which have been extrapolated in the UV and IR wavelengths domain by using the synthetic spectra from the GISSEL library (Charlot and Bruzual, 1996). In order to reproduce observed colors bluer than the Irr template, we add two spectra of star-forming galaxies computed with the GISSEL model for solar metallicity, Salpeter IMF, constant star formation rate and 0.05 and 2 Gyears old. Following the approach adopted by Sawicki et al. (1997), we have interpolated between the 6 original SEDs in order to provide a finer grid of the spectral-type coverage with a total number of 61 templates. To illustrate the differences between the various SEDs, in Figure 1 we show the k-corrections in the R passband as a function of redshift. In this figure the k-corrections are computed by using the global instrument throughput of the filter curves and by including the absorption by intergalactic medium as given by Madau (1995).

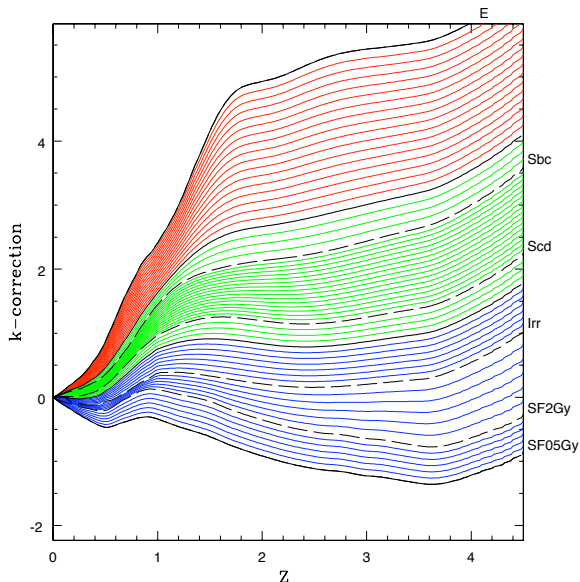


**Fig. 1.** k-correction in R passband for the different SEDs. The dashed lines represent the SEDs of an Elliptical, Sbc, Scd and Irr from Coleman et al. (1980) and the continuously star forming galaxies 0.5 and 2 Gyars old based on the GISSSEL library. The solid lines show the transition SEDs between the three spectral classes used in the Luminosity Function (see text).

## 2.2. The luminosity function

### 2.2.1. the adopted Luminosity function parameters

To derive the density of objects inside a given magnitude and redshift ranges, we need the knowledge of the luminosity function per spectral type. We decide to use the luminosity function measured from the ESO-Sculptor Survey (de Lapparent et al., 2002, hereafter ESS) covering an area of  $\simeq 0.4 \text{ deg}^2$ . The spectroscopic completeness of the ESS is 100%, 90% and 45% at  $R_c \leq 20, 20.5$  and 21 respectively. One of the advantage of this luminosity function is that it provides the luminosity function parameters for three spectral classes (Early-type, Spiral and irregular) and their redshift evolutions up to  $z \simeq 0.6$ . To describe the luminosity and density redshift evolution we adopt the following forms :  $M_*(z) = M_* + M_{ev}(z)$  and  $\phi_*(z) = \phi_* \times \phi_{ev}(z)$  respectively.

The observed LFs of the ESS do not show any evolution for the Early and Intermediate classes while for the Late class an evolution is observed in the redshift range  $0.15 \leq z \leq 0.6$  which can be well fitted by a density evolution as shown in Table 1.

Beyond the spectroscopic limits of the ESS ( $z \simeq 0.6$ ), the evolution of the luminosity function is poorly constrained due to the small numbers of existing deep fields which have large uncertainties making difficult to disentangle the individual evolution of the three Schechter parameters ( $\alpha, \Phi_*, M_*$ ). Therefore we decide to derive a simple form of evolution which can reproduce the redshift distributions ( $N(z)$ ) for moderately deep surveys as discuss below. Note that our goal is not to provide any constraint on the cosmological parameters or galaxy evolution but to insure that we can reproduce in

addition to the  $N(z)$ , the number counts and color distributions.

To derive the evolution of the luminosity function which can reproduce the  $N(z)$ , we make several assumptions :

- The LF derived in the ESS does not change with  $z$  for the Elliptical and Intermediate classes.
- The slope  $\alpha$  does not change with  $z$  for the three classes
- At  $z \geq 0.7$ , the density evolution for the late class is frozen
- A luminosity evolution is added ( $M_{ev}(z)$ ) for redshifts  $z \geq 1.25$  as specified in Table 1
- The range of SED for the late type is progressively shifted near “youngest” spectral type at increasing  $z$

The LF parameters adopted in our simulations are given in table 1. In column (1) we indicate the spectral class, in column (2) the SED’s intervalle corresponding to our numerology where the original SEDs from Coleman et al. (1980) refer to: Elliptical=1, Sbc=22, Scd=38 and Irr=49 and the two star-forming galaxies refer to: SF2Gy=55 and SF0.5Gy=61. The redshift range where the parameters are valid are given in column (3). The ESS’s Schechter parameters:  $\phi_*$ ,  $\alpha$ ,  $R_*$  are given in Column (4), (5) and (6) respectively. Note that  $R_*$  value quoted here refers to the Vega system. The density and luminosity redshift evolution:  $\phi_{ev}(z)$ ,  $M_{ev}(z)$  are given in columns (7) and (8) respectively.

### 2.2.2. The predicted redshift distribution

In Fig 2, 3 we show the  $N(z)$  for the whole sample (solid lines) and for the three spectral classes (Early-type class:short dashed lines; Intermediate class:long dashed line; Late-type class:dot-short dashed line) at different magnitude limits as predicted by the LF parameters described in table 1. The simulation covers an area of  $0.25 \text{ deg}^2$  and the dashed region for the entire sample corresponds to the  $2\sigma$  Poisson uncertainties.

In Fig 2 upper panel, we show the  $N(z)$  corresponding to the depth of the ESS with galaxies brighter than  $R_{vega} \leq 20.5$  (or  $R_{AB} \leq 20.7$ ). The global  $N(z)$  is similar to the observed one with a peak at  $z_{peak} \sim 0.25$  and a tail vanishing at  $z \sim 0.6$ . The values of  $z_{peak}$  change according to the considered spectral class with an higher value for elliptical class ( $z_{peak} \sim 0.35$ ) than for the Intermediate class ( $z_{peak} \sim 0.3$ ) and Irregular class ( $z_{peak} \sim 0.2$ ). Lower  $z_{peak}$  is obtained for Irr because of the fainter value of  $R_*$  (see Table 1).

In Fig 2 lower panel, we show the predicted  $N(z)$  for  $17.5 \leq I_{AB} \leq 22.5$  similar to the CFRS (Lilly et al., 1995). The CFRS median redshift is  $z_{med} = 0.56$  and a fraction of 4% of the galaxies has a redshift higher than  $z \geq 1$  (Crampton et al., 1995). Our predicted  $N(z)$  gives a  $z_{med} = 0.53$  with a fraction of 6% of galaxies at  $z \geq 1$ . As mentioned by Crampton et al. (1995), a significant fraction of high- $z$  old galaxies has not been spectroscopically confirmed which could increased their estimates.

In Fig 3 we show the  $N(z)$  for the magnitude range  $22 \leq I_{AB} \leq 25$  (upper panel) and  $22 \leq B_{AB} \leq 26$  (upper panel). The Irregular classe is dominant with respect to the two others and shows a tail at high redshift due to the small k-correction for this class and to the inclusion of luminosity evolution at high

**Table 1.** Adopted luminosity function in the R band (in Vega system) from ESO-Sculptor (see text) and at higher redshifts.

LF class	Type Range	z range	$\phi_*$	$\alpha$	$R_*$	$\phi_{ev}(z)$	$M_{ev}(z)$
Early	1 – –18	$0 \leq z \leq 6$	$14.77 \times 10^{-3}$	0.11	-20.56	1	0
Spiral	16 – –42	$0 \leq z \leq 6$	$13.54 \times 10^{-3}$	-0.73	-20.43	1	0
Late/Irr	36 – –55	$0 \leq z \leq 0.15$	$6.06 \times 10^{-3}$	-1.63	-19.84	1	0
Late/Irr	40 – –57	$0.15 < z \leq 0.7$	$6.06 \times 10^{-3}$	-1.63	-19.84	$(1 + (z - 0.15) \times 3.69)$	0
Late/Irr	40 – –57	$0.7 < z \leq 1.25$	$16.12 \times 10^{-3}$	-1.63	-19.84	1	0
Late/Irr	40 – –59	$1.25 < z \leq 2.5$	$16.12 \times 10^{-3}$	-1.63	-19.84	1	$-0.12 * (z - 1)$
Irr	42 – –62	$2.5 < z \leq 3.5$	$1.6 \times 10^{-2}$	-1.63	-19.84	1	$-0.22 * (z - 1)$
Irr	42 – –62	$3.5 < z \leq 6$	$1.6 \times 10^{-2}$	-1.63	-19.84	1	$-0.12 * (z - 1)$

z. The global predictions give a good fit to the  $N(z)$  based on photometric redshifts in the HDF-South and North (Arnouts et al., 1999, 2001). The HDF values (filled points) are shown with Poissonian errorbars.

Our empirical approach to define the luminosity function allows us to get a reasonable description of the relative fraction of galaxies at low and high redshifts which is a preliminary step to reach one of our objective in quantifying the contamination effects of selected targets based on color-color diagrams.

### 2.3. Observational conditions

In order to provide realistic simulated catalogues, we need to match the observational conditions of one survey as well as a realistic magnitude estimates for the sources. To reach this goal, we assume that the main parameters to describe a survey are the following: the surface brightness and seeing condition in each passband, the physical galaxy sizes for various types and redshifts.

#### 2.3.1. Galaxy luminosity profiles

To describe the luminosity profile of elliptical and disk galaxies we adopt the formalism of Yosshi (1993). A simple function with an index of integer n is used

$$g(\beta) = g_0 \exp(-a_n \beta^{1/n}) \quad (1)$$

where  $g_0$  is the central luminosity and  $\beta = r/r_e$  with  $r_e$  corresponding to the effective radius enclosing half of the total luminosity. For an elliptical profile,  $n = 4$  and  $a_4 = 7.67$  and for an exponential profile,  $n = 1$  and  $a_1 = 1.68$ . Note that often for disks a scale length parameter  $r_h$  is used instead of  $r_e$ . They are related by  $r_e = a_1 r_h = 1.68 r_h$ .

#### 2.3.2. convolution by the Point Spread Function

The galaxy models are convolved with a circular gaussian PSF which matches the observational conditions. The one dimension profile convolved by a PSF with a dispersion  $\sigma$  is defined as :

$$\tilde{g}(\sigma, \beta) = \sigma^{-2} f(\beta) \int_0^\infty g(\xi) I_0(\beta \xi / \sigma^2) f(\xi) \xi d\xi \quad (2)$$

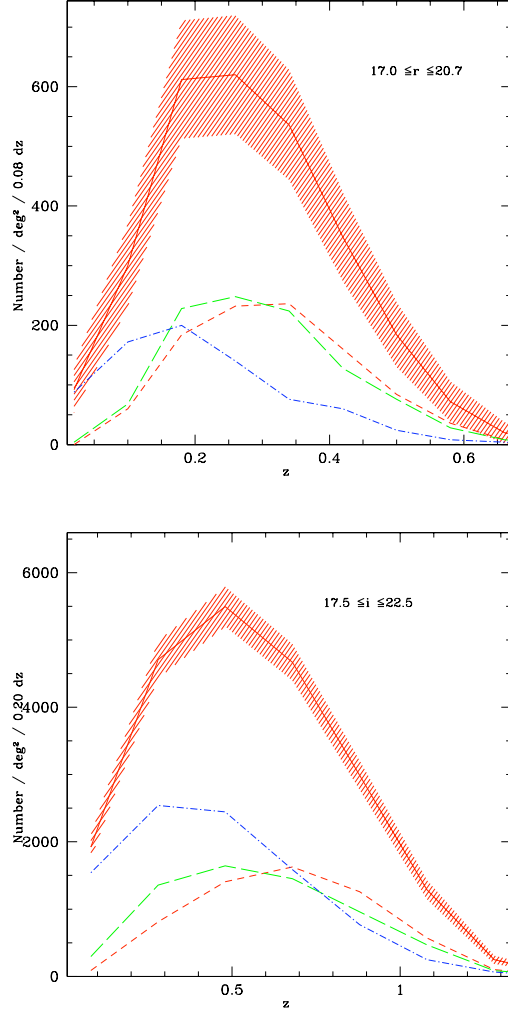


**Fig. 2.** Redshift distribution  $N(z)$  for different limiting magnitude samples:  $17 \leq R_{AB} \leq 20.7$  (upper panel) similar to the ESO Sculptor Survey and  $17.5 \leq I_{AB} \leq 22.5$  (lower panel) similar to the CFRS. The dashed regions represent the global  $N(z)$  with  $2\sigma$  poisson uncertainties based on simulated catalogue covering  $0.25 \text{ deg}^2$ . The short dashed lines represent the elliptical class, the long dashed line represents the Intermediate class and the dot-short dashed line the Irregular class.

where  $I_0(x)$  is the modified Bessel function of the first kind and

$$f(x) = \exp(-x^2/2\sigma^2) \quad (3)$$

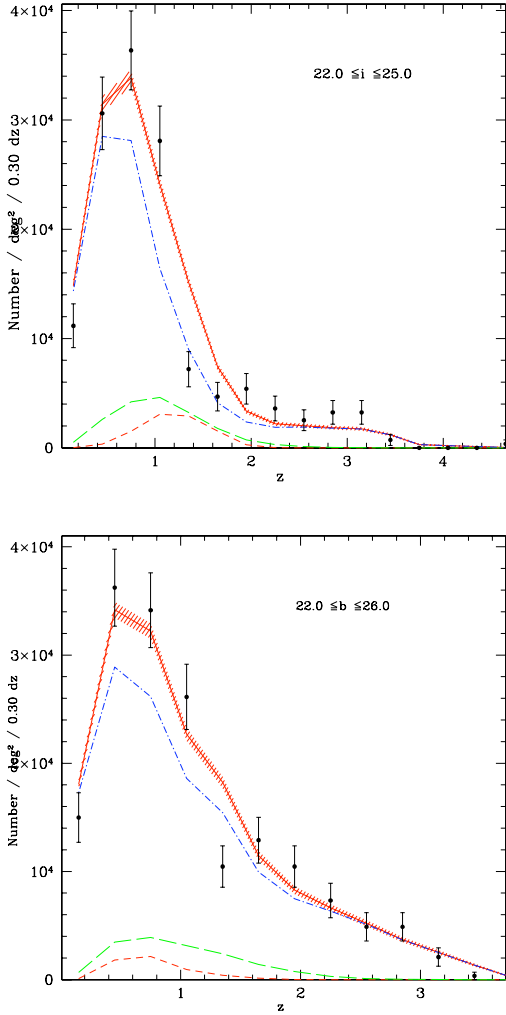


**Fig. 3.** Same as Figure 2 for magnitude range :  $22 \leq I_{AB} \leq 25$  (upper panel) and  $22 \leq B_{AB} \leq 26$  (lower panel). The predicted  $N(z)$  are compared with the averaged  $N(z)$  from the HDF-North and South (points with poissonian errorbars) based on photometric redshifts.

The seeing FWHM is related to the dispersion  $\sigma$  as in Yoshii (1993) by :

$$\text{seeing FWHM (arcsec)} = 2.35 \left( \frac{r_e}{d_A} \right) \sigma \text{Conv} \quad (4)$$

where  $d_A$  is the angular distance and  $\text{Conv}$  is a conversion factor from radian to arcsec ( $\text{Conv} = 180 \times 3600 / \pi$ ). The integrated luminosity profile out to  $\beta$  is given by:

$$\tilde{G}(\sigma, \beta) = 2\pi \int_0^\beta \tilde{g}(\sigma, \xi) \xi d\xi \quad (5)$$

To speed up the calculation, the functions  $\tilde{g}(\sigma, \beta)$  and  $\tilde{G}(\sigma, \beta)$  have been computed by using a grid of  $0 \leq \beta, \sigma \leq 20$  with steps of 0.1 in  $\beta$  and  $\sigma$  as in Ferguson and Mc Gaugh (1994).

### 2.3.3. surface brightness definition

The angular size  $\theta$  for a galaxy with a radius  $R$  at a redshift  $z$  corresponds to :

$$\theta(\text{arcsec}) = R/d_A \text{Conv} = R(1+z)^2/d_L \text{Conv} \quad (6)$$

where  $d_L$  is the distance luminosity. This implies that the surface brightness diminishes as  $(1+z)^4$  with increasing redshift. The surface brightness ( $\text{mag.arcsec}^{-2}$ ) for a galaxy in a given passband and redshift  $z$  is then given by :

$$\mu(\theta, z) = \mu_0 - 2.5 \log \left[ \frac{\tilde{g}(\beta, \sigma)}{g_0} \right] + 10 \log(1+z) + (k+e)(z) \quad (7)$$

where  $\mu_0$  is the central surface brightness and  $(k+e)(z)$  is the  $k$  correction and evolution correction for a given galaxy in the passband. The total luminosity for a galaxy is related to the effective radius  $r_e$  (Disney and Phillipps, 1983) by:

$$L_{\text{tot}} = \frac{(2n)! \pi}{a_n^{2n}} g_0 r_e^2 \quad (8)$$

The central surface brightness corresponds to :

$$\begin{aligned} \mu_0(\text{mag.arcsec}^{-2}) &= M_{\text{abs}} - 5 + 5 \log(r_e[\text{pc}]) \\ &\quad - 2.5 \log \left( \frac{a_n^{2n}}{(2n)! \pi} \right) + 5 \log(\text{Conv}) \end{aligned} \quad (9)$$

For an elliptical galaxy this corresponds to :

$$\mu_0 = M_{\text{abs}} + 5 \log(r_e[\text{pc}]) + 16.63 \quad (10)$$

and for a disk galaxy :

$$\mu_0 = M_{\text{abs}} + 5 \log(r_e[\text{pc}]) + 22.44 \quad (11)$$

### 2.3.4. The size-luminosity relations

The relationships between the effective radii for disks and ellipticals and the absolute magnitude have been established in the B band for local galaxies. We use the notation adopted by Yoshii (1993):

$$-M_{\text{abs}} = p \log(r_e[\text{kpc}]) + q + (p-5) \log \left( \frac{H_0}{50} \right) \quad (12)$$

In Table 2, we report the different values for  $p$  and  $q$  parameters based on the works of Binggeli et al. (1984) in the case of ellipticals and Freeman (1970) for the disks. For the disks, we adopt the Freeman law  $\mu_0(B) = 21.65$  for non-dwarf galaxies ( $M_{\text{abs}} \leq -17$ ) otherwise we assume  $\mu_0(B) = 21.65 + 0.7(M_{\text{abs}} + 17)$ . Finally a dispersion around the adopted surface brightness relation is applied by adding a gaussian distribution with  $\sigma_{\mu_0} = 0.35$  to the mean.

Note that based on a large sample of local spiral galaxies by de Jong and Lacey (2000) have shown that a better parametrisation of the relationship between the luminosity and scale size can be obtained by adopting a lognormal distribution but we still use the approach described above since this will not affect the purpose of this work. To parametrize the redshift evolution of the galaxy size-Luminosity relation for disk galaxies we refer to the previous works based on CNOC survey and HST imaging

**Table 2.** Adopted relationship between absolute B magnitude  $B_{ABS}$  and effective radius  $r_e$

Type	p	q	$B_{ABS}$ range
Ellipticals	10	15.5	$-20.5 \leq B_{ABS} \leq -12$
	3.33	18.833	$-23 \leq B_{ABS} < -20.5$
Disks	16.67	12.97	$-17 < B_{ABS}$
	5	15.79	$B_{ABS} \leq -17$

of the CFRS (Schade et al., 1995, 1996) for the bright end of the B band luminosity function up to  $z \sim 1.2$  and for the faint-end of the LF we use the works based on deep field surveys (NTT Deep Field and HDF fields) in the range  $0.4 \leq z \leq 3.5$  by Poli et al. (1999) and Giallongo et al. (2000). While one can not disentangle between size and luminosity evolution, in this work we adopt a galaxy-size evolution with  $z$  assuming a simple parametrisation as follows:  $r_e(z) = r_e(z=0) (1+z)^{-\eta}$ . Note that for the early-type galaxies we do not include any evolution.

Based on analysis of disk galaxies in the field and clusters, Schade et al. (1995, 1996) have observed a brightening of the central surface brightness  $\mu_0$  at increasing redshift which corresponds to  $\Delta\mu_0(B) \sim -0.6, -1.2$  for the intervals  $0 \leq z \leq 0.5$  and  $0.5 \leq z \leq 1.2$ . The amplitude of  $\Delta\mu_0(B)$  vs  $z$  is illustrated in Figure 2 from Schade et al. (1996). This can be well reproduced with our parametrization by adopting  $\eta = 1.2$ .

Adopting this relation for the entire redshift range, in Figure 4, we show the scale length  $r_h$  (for disks) distributions for various B band luminosities (specified in each panel) and redshift ranges ( $z \leq 0.3$ : solid lines;  $0.3 \leq z \leq 1$ : dashed lines;  $1 \leq z \leq 3.5$ : dot-dashed lines). Only simulated galaxies with  $R_{AB} \leq 26$  are shown. Inside a luminosity range, the scale lengths ( $r_h$ ) decrease with increasing redshift and for a fixed redshift range,  $r_h$  decrease towards the fainter luminosities. Our simulated galaxy sizes are in good agreement with the observed ones from deep fields by Giallongo et al. (2000). For  $0.4 \leq z \leq 1$ , Giallongo et al. found that the  $r_h$  distribution span the range  $0.8 \leq r_h \leq 6$  kpc with a peak at  $r_h \sim 2$  kpc for  $-21 \leq B_{abs} \leq -19$  and  $0.2 \leq r_h \leq 4$  with a peak at  $r_h \sim 1 - 1.2$  kpc for  $-19 \leq B_{abs} \leq -17$  consistent with our estimates. For  $1 \leq z \leq 3.5$ , they found that the  $r_h$  distribution span the range  $0.2 \leq r_h \leq 6$  kpc with a peak at  $r_h \sim 1 - 1.5$  kpc for  $-22 \leq B_{abs} \leq -19$  again consistent with our estimates.

### 2.3.5. apparent magnitude estimates

Knowing the luminosity profile of the galaxies we can measure the apparent magnitude by integrating the profile of a galaxy at a given  $z$  up to a given angular size  $\theta$  defined as :

$$m(\theta) = M_{abs} - 5 + 5 \log(d_L) + (k+e)(z) - 2.5 \log \left[ \frac{\tilde{G}(\beta)}{\tilde{G}(\infty)} \right] \quad (13)$$

The choice of  $\theta$  depends on the scheme adopted in the observations to measure the magnitudes. In the following we define four kinds of magnitudes:

- A pseudo-isophotal magnitude defined as  $\theta = k \times \theta_{iso}$  where  $\theta_{iso}$  is the isophotal angular size defined by equating

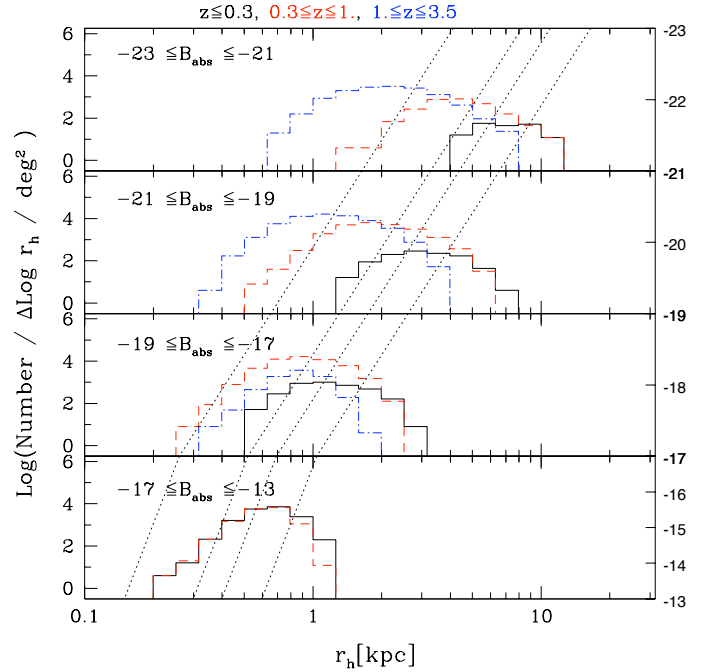


**Fig. 4.** Behaviour of the scale length  $r_h$  distributions with  $z$  (histograms) as a function of  $B_{ABS}$  (different panels) for disk galaxies. The different histograms correspond to:  $0 \leq z \leq 0.3$  (solid lines),  $0.3 \leq z \leq 1$ . (dashed lines),  $1. \leq z \leq 3.5$  (dot-dashed lines). The dotted lines show the adopted relationship between  $r_e$  and  $B_{ABS}$  for  $z = 0$  (Freeman law, right line) and  $z = 0.5, 1, 3$  (from right to left respectively). Only shown are galaxies with  $R_{AB} \leq 26$ .

Eq 7 to the value of the observed surface brightness limits. The pseudo-isophotal magnitude is computed by enlarging  $\theta_{iso}$  with a fixed factor  $k$  with  $k = 1$  corresponding to the standard isophotal magnitude.

- An adaptive magnitude as defined by Kron (1980) and Bertin & Arnouts (1996). First, a characteristic radius is computed using the modulus of the first moment of the light distribution  $\theta_k = \sum \theta \tilde{g}(\theta) / \sum \tilde{g}(\theta)$ . The magnitude is computed inside an enlarged radius by  $\theta = k \times \theta_k$ . A good compromise between total magnitudes and noise is obtained with  $k \sim 2.5$  (Bertin & Arnouts, 1996). As implemented in the SExtractor software for the parameters ( $MAG - AUTO$ ), we impose  $\theta \geq 1.6 \times \theta_{iso}$ .
- A petrosian magnitude (Petrosian 1976, Shimasaku et al., 2001) which is defined as the ratio ( $\eta$ ) between the surface brightness at a given radius  $\theta_p$  and the mean surface brightness averaged over the interior area enclosed by  $\theta_p$ :

$$\eta = \frac{\tilde{g}(\theta_p)}{\tilde{G}(\theta_p) / \pi \theta_p^2} \quad (14)$$

For each galaxy, we compute  $\theta_p$  from Eq 14 by adopting  $\eta = 0.2$ . The petrosian magnitude is then obtained by integrating the flux inside a radius  $\theta = 2 \times \theta_p$ .

- An aperture magnitude measured inside a fixed radius  $\theta = constant$

We can estimate the errors for each magnitude as defined by Bertin & Arnouts (1996) :

$$\Delta m = 1.0857 \frac{\sqrt{A(ff\sigma)^2 + \frac{F}{g}}}{F} \quad (15)$$

where  $A$  is the area (in pixels) estimated according to the magnitude scheme used,  $F$  is the total flux (adu),  $\sigma$  is the standard deviate of noise (adu),  $g$  is the gain ( $e^-/adu$ ) and  $ff$  is a fuge factor if the resulting images are stacked by using non linear process resulting in a correlation of the noise properties. This estimate requires some additional information relative to the observations like zero-points, pixel-scales, gain and fuge-factor. Note that following this equation, in the background limited regime, the errors are not sensitive to the gain.

#### 2.4. Generation of mock catalogue

Finally to generate the simulated catalogues we proceed in several steps :

- We derive the expected number of objects in a given area  $N_{gal}(\Delta m, \Delta z, type)$  inside a shell of apparent magnitude and redshift for each SED and neglecting observational effects (ideal case). The reference magnitude corresponds to the passband where the LF is defined (in our case  $R$  band). The number of observed galaxies is obtained from a Poisson deviated distribution centered on  $N_{gal}$ . According to the used SED, we derive the magnitudes in all the other passbands which includes the appropriated ( $k + e$ ) corrections.
- For each generated object, the “observed” magnitudes are obtained by taking into account the luminosity profile of the galaxy and observational conditions (seeing, SB limits) and computing the fraction of light lost according to the magnitude scheme described in section 2.3.5. We assume that the early-type classe is dominated by de Vaucouleur profiles ( $n = 4$ ) and the Intermediate and late-type classes by exponential profiles ( $n = 1$ ). Objects with angular sizes  $2\theta < D_{min}$  in a given passband are considered as undetected and the magnitudes are set to the upper-limit in this band. In our case the minimum diameter has been imposed to be  $D_{min} = 0.8 \times \text{seeing FWHM}$ .
- The final “observed” magnitudes include a gaussian deviation according to the errors. The photometric errors are either derived from the observation themselves or estimated by using the Equation 15. Objects with magnitudes fainter than the  $2\sigma$  magnitude limit in a given passband are replaced by upper-limits.

##### 2.4.1. limitation of our method

In this simplistic model we made several assumptions :

- Galaxies are circular which mean that we do not include spheroidal flattening for elliptical profiles and disk inclination for exponential profile (disks seen face-on). For disk galaxies, magnitude estimates can be considered as pessimistic since the surface brightness is increased when a disk is seen edge-on.

**Table 3.** Observational parameters

Band	Seeing (arcsec)	$\mu_{lim}$ (in AB) (mag/arcsec <sup>2</sup> )
U	1.03	26.8
B	1.02	27.1
V	0.97	26.1
R	0.90	26.1
I	0.93	25.2

- We also do not include any bulge-to-disk ratio which has been agreed by Yoshii (1993) to be a reasonable assumption whence you are probing relatively high redshift galaxies.
- Our SED template is rather crude and we are not proposing to built simulation to reproduce peculiar objects but to get a description of the global population with “standard” spectral energy distribution. For instance, we assume that galaxies do not show any color gradients from center to border since a single SED is used for each galaxy. The impact of dust extinction is not simulated and can only be roughly reflected in our simulation by using the interpolated SED between the 6 original SEDs.
- When we are computing magnitudes, we assume that the galaxy profile is perfectly known which is not the case in practice since the measurement can be extremely noisy specially for faint sources before the seeing dominated regime.

Nevertheless this empirical simulations are helpfull to address some general characteristics specific to a given survey like for instance the relative biases of different magnitude schemes and the efficiency of a given survey to select specific targets as we will discuss in the next sections.

### 3. The relative behaviours of the estimators in realistic conditions

We have generated the mock catalogues based on the observational conditions of the EIS data in the CDF-South. In Table 3, we show the observational parameters used for generating the mock catalogue. Column (1) shows the filter passband, column (2) the seeing in arcsec and column (3) the surface brightness.

#### 3.1. The apparent galaxy sizes

#### 3.2. The performance of the magnitude estimators

In this sections we show the behaviour of the different magnitude estimators with respect to the total magnitudes according to the observational conditions described in Table 3. In Fig 6 we compare the difference between the simulated and the total magnitudes ( $\Delta mag$ ) in the  $R$  band as a function of the total  $R$  magnitude and redshift  $z$  for the pseudo-isophotal magnitude defined with  $k = 1.6$  (top panels), the adaptive magnitude with  $k = 2.5\theta_k$  ( $2^{nd}$  panels), the fixed aperture magnitude with  $\theta = 3arcsec$  ( $3^{rd}$  panels) and the petrosian magnitude with  $\eta = 0.2$  (bottom panels). The median differences ( $\Delta mag$ ) and the  $1\sigma$  r.m.s. are shown separately for the three galaxy classes of the luminosity function. The elliptical class is shown

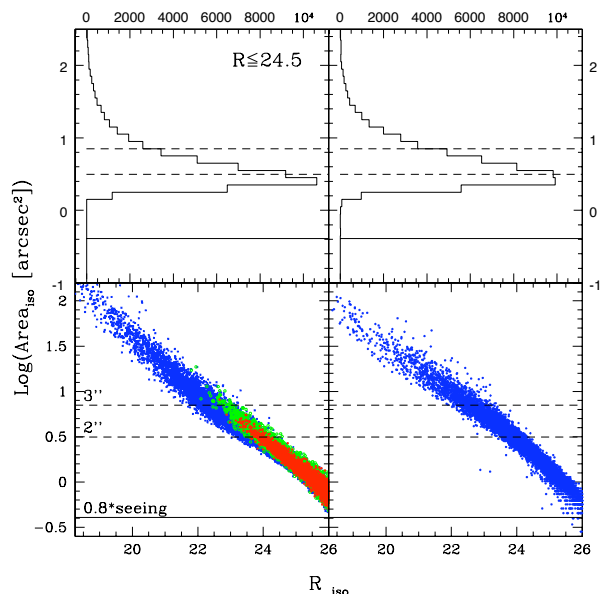


**Fig. 5.** Behaviour of the apparent galaxy sizes with magnitude ( $R$ ).

with red filled circles, the intermediate class with green open circles and the late-type class with blue filled triangles. In Fig 9, we compare  $\Delta mag$  in  $B$  band (upper panels) and  $I$  band (lower panels) as a function of the total magnitude for the adaptive magnitudes (left panels) and petrosian magnitude (right panels).

### 3.3. The impact in the color estimates

### 3.4. Towards an optimal magnitude schemes

## 4. Application to the EIS CDF-S data

### 4.1. Comparison of the number counts

### 4.2. Comparison of the optical-colors

### 4.3. Application to the high-z galaxy population

*Acknowledgements.* We would like to thank xxx

## References

- Arnouts S., de Lapparent V., Mathez G., *et al.*, 1997, A&AS, 124, 163  
 Arnouts S., d’Odorico S., Cristiani S., *et al.*, 1999, A&A, 341, 641  
 Arnouts S., *et al.*, 2001, A&A, in press, astro-ph/0103071  
 Bertin E., Arnouts S., 1996, A&AS, 117, 393  
 Bertin, E., 1998, SExtractor, User’s guide, v2.0

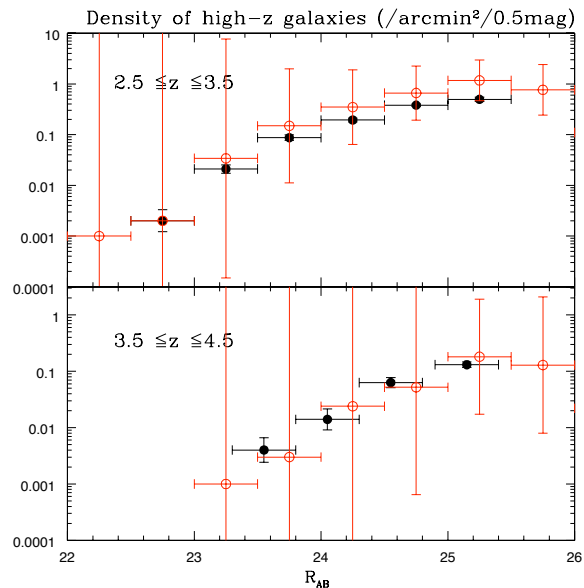


**Fig. 12.** Comparison of the predicted High-z galaxy density (red open circles) as a function of magnitude with the spectroscopically confirmed density from Steidel et al. (solid circles). Errorbars show the  $1\sigma$  poissonian fluctuation.

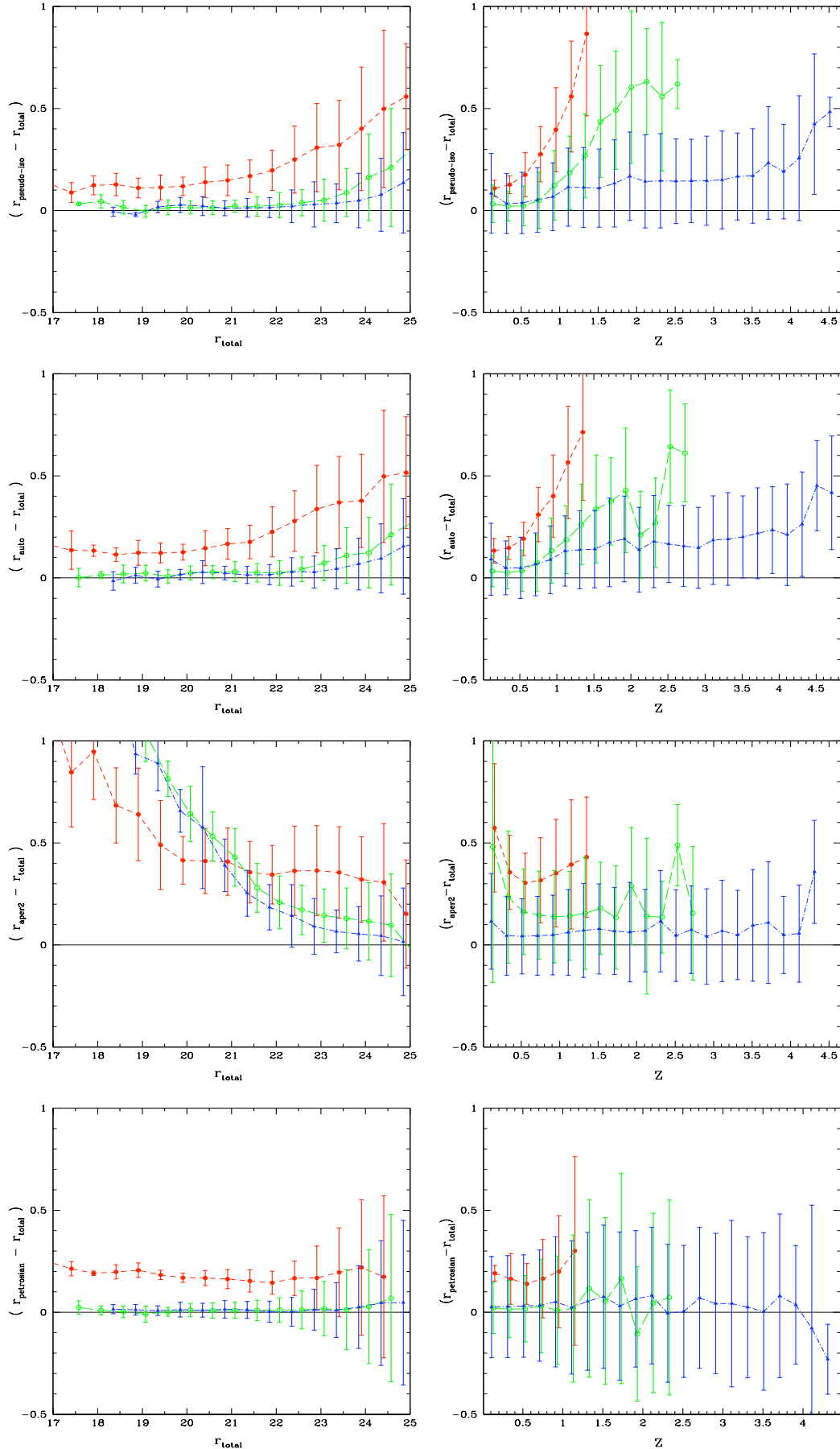


**Fig. 6.** Comparison between the simulated and total  $R$  magnitudes for  $R_{total} \leq 25$  as a function of ideal  $R$  magnitude (left panels) and redshift (right panels) for different magnitude schemes: Pseudo-isophotal (with  $k = 1.6$ , top panels); adaptive ( $2^{nd}$  panels); fixed apertures with 3arcsec diameter ( $3^{rd}$  panels); Petrosian magnitude (with  $\eta = 0.2$ , bottom panels). The comparisons are shown for the three spectral classes: Early types (filled circles), Intermediate types (open circles) and late types (filled triangles). The errors are the  $1\sigma$  dispersion around the medians.

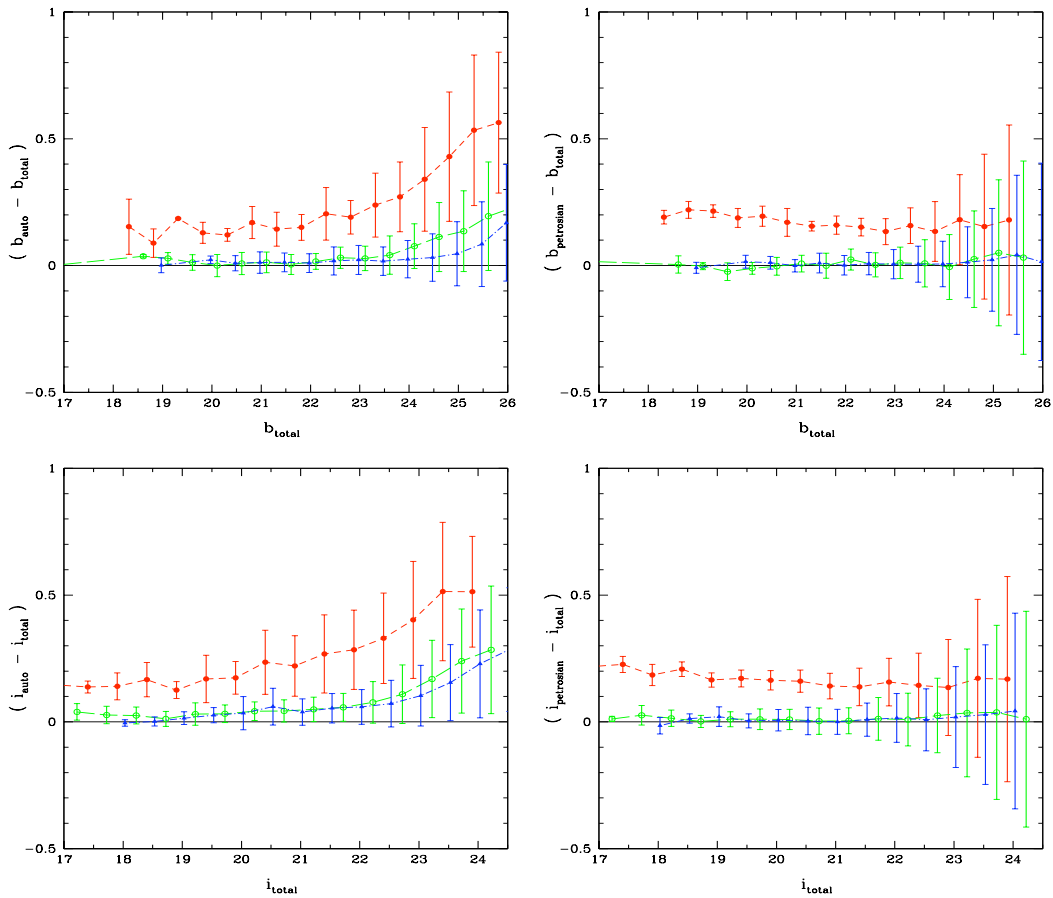


**Fig. 7.** Comparison between simulated and total magnitudes for the adaptive magnitude (left panels) and Petrosian magnitude (right panels) in the B band (with  $B_{total} \leq 26$ , upper panels) and the I band (with  $I_{total} \leq 24.5$ , lower panels). The symbols are the same as in the Fig 6.

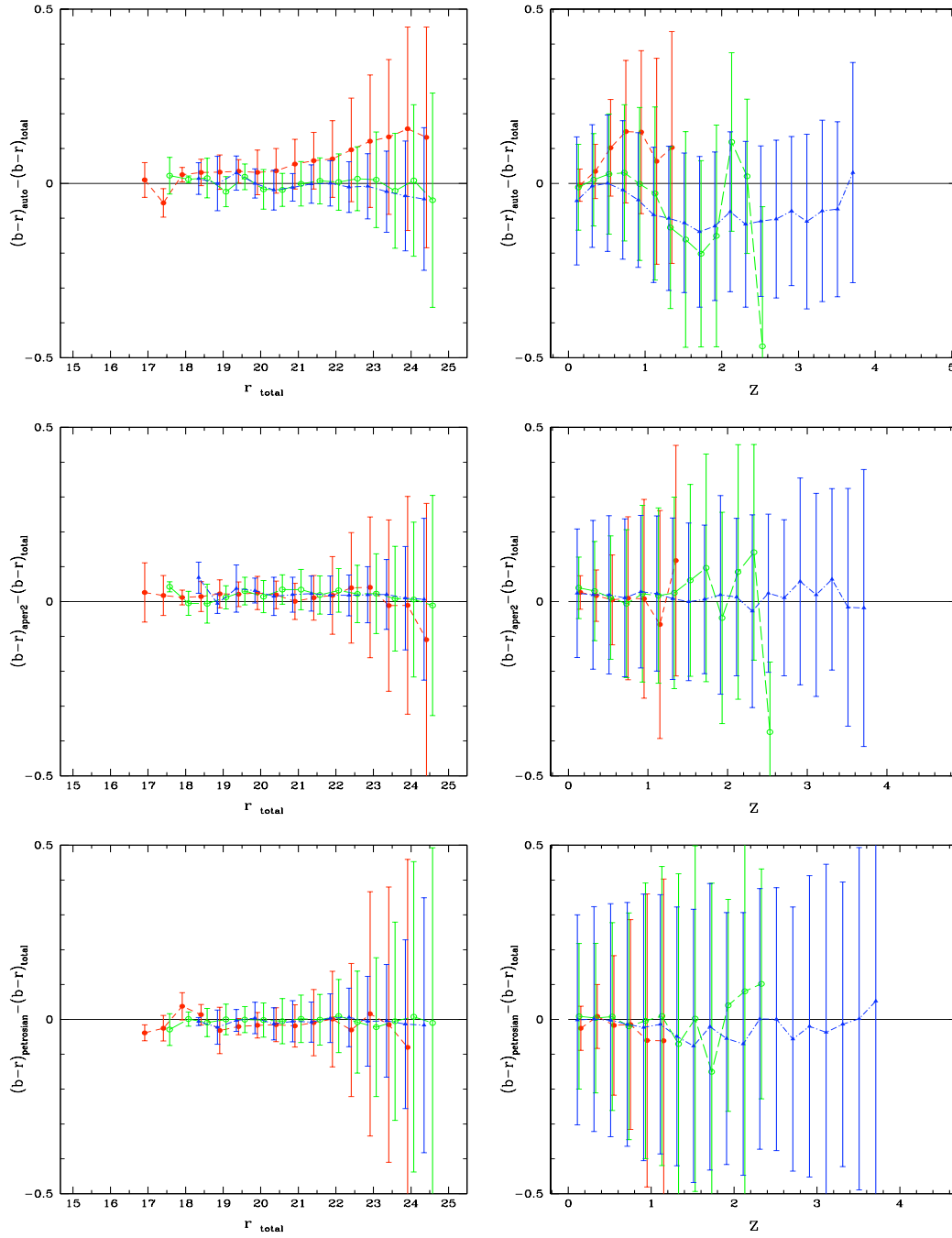


**Fig. 8.** Comparison between simulated and total colors ( $B-R$ ) for  $R_{\text{total}} \leq 25$  as a function of ideal  $R$  magnitude (left panels) and redshift (right panels) for different magnitude schemes: adaptive (top panels); fixed apertures with 3arcsec diameter ( $2^{\text{nd}}$  panels); Petrosian magnitude (with  $\eta = 0.2$ , bottom panels). The symbols are the same as in the Fig 6.

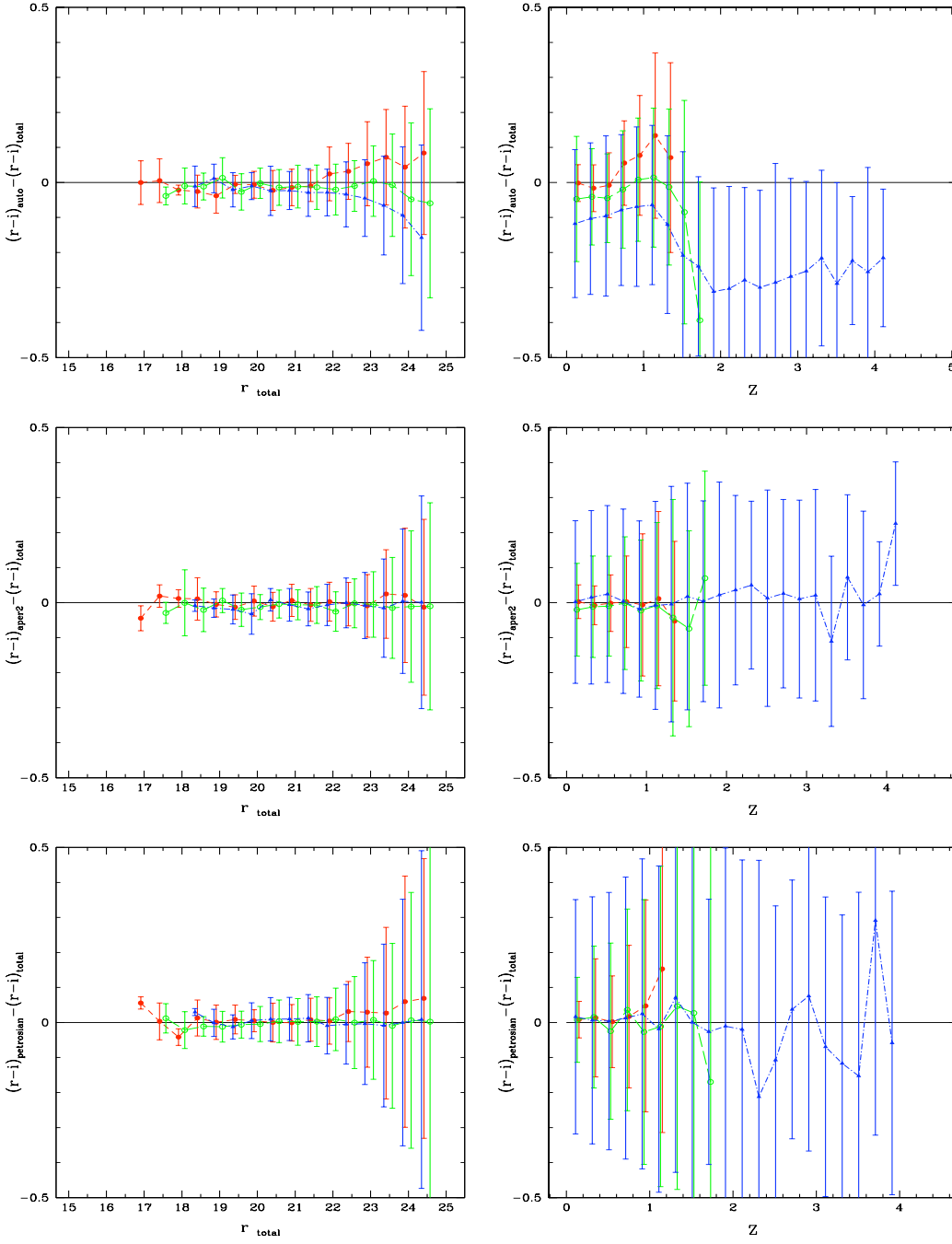


**Fig. 9.** Comparison between simulated and ideal colors ( $R - I$ ) for  $R_{\text{total}} \leq 25$  as a function of ideal  $R$  magnitude (left panels) and redshift (right panels) for different magnitude schemes: adaptive (top panels); fixed apertures with 3arcsec diameter ( $2^{\text{nd}}$  panels); Petrosian magnitude (with  $\eta = 0.2$ , bottom panels). The symbols are the same as in the Fig 6.

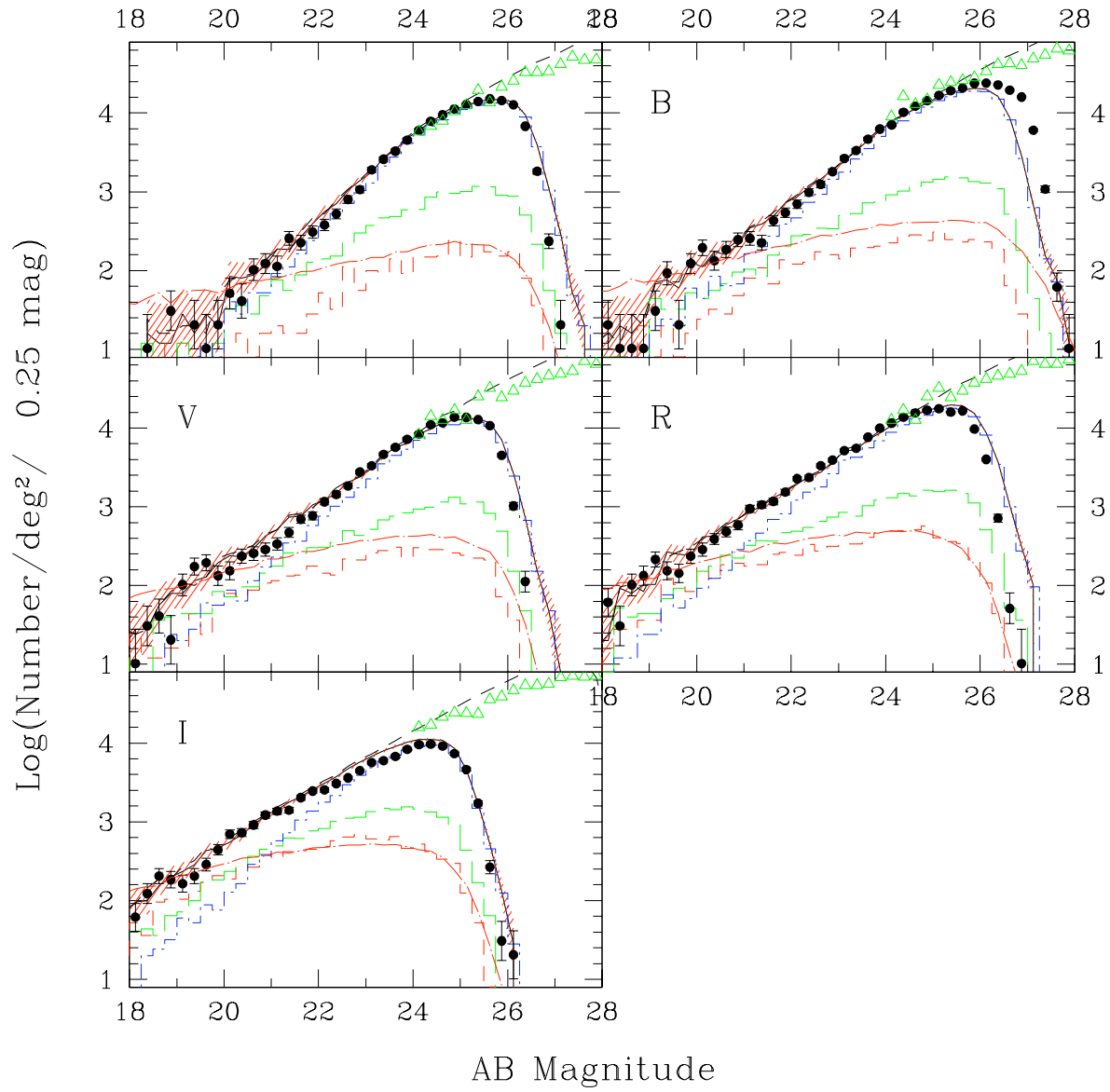


**Fig. 10.** Comparison of the differential Number count from U to I band in AB system. The observations come from the D2c (filled circles). The simulated catalogue is shown with solid lines and the dashed areas correspond to the  $2\sigma$  poisson fluctuations. The short dashed lines show the number counts neglecting observational effects. The long dashed-dotted lines show the simulated star number counts.

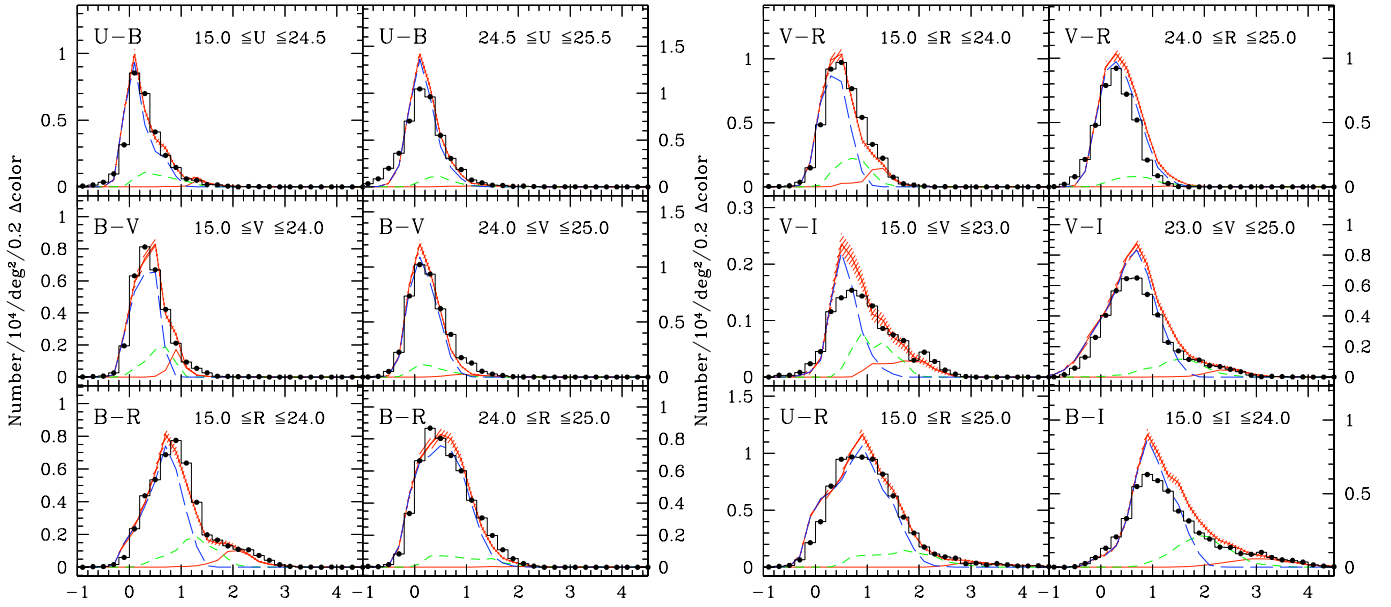


**Fig. 11.** Comparison of the predicted color distribution (red lines) with the observed one from CDF-S (blue histograms). The shaded regions corresponds to  $2\sigma$  poissonian fluctuations.

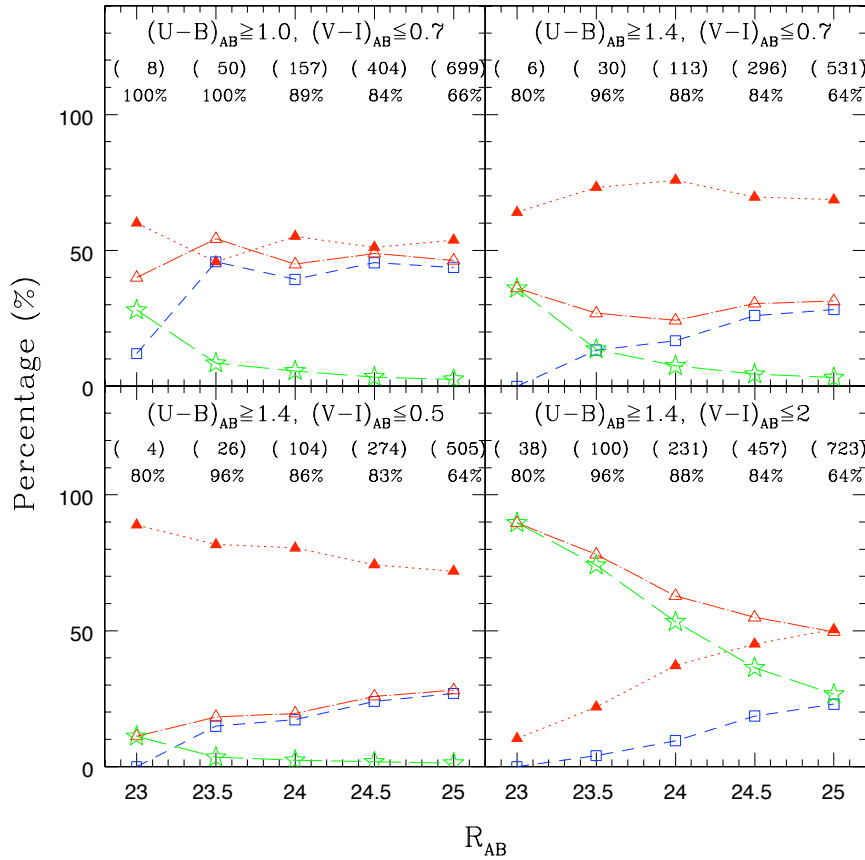


**Fig. 13.** Effect of selection criteria for the boxes of LBGs and interlopers

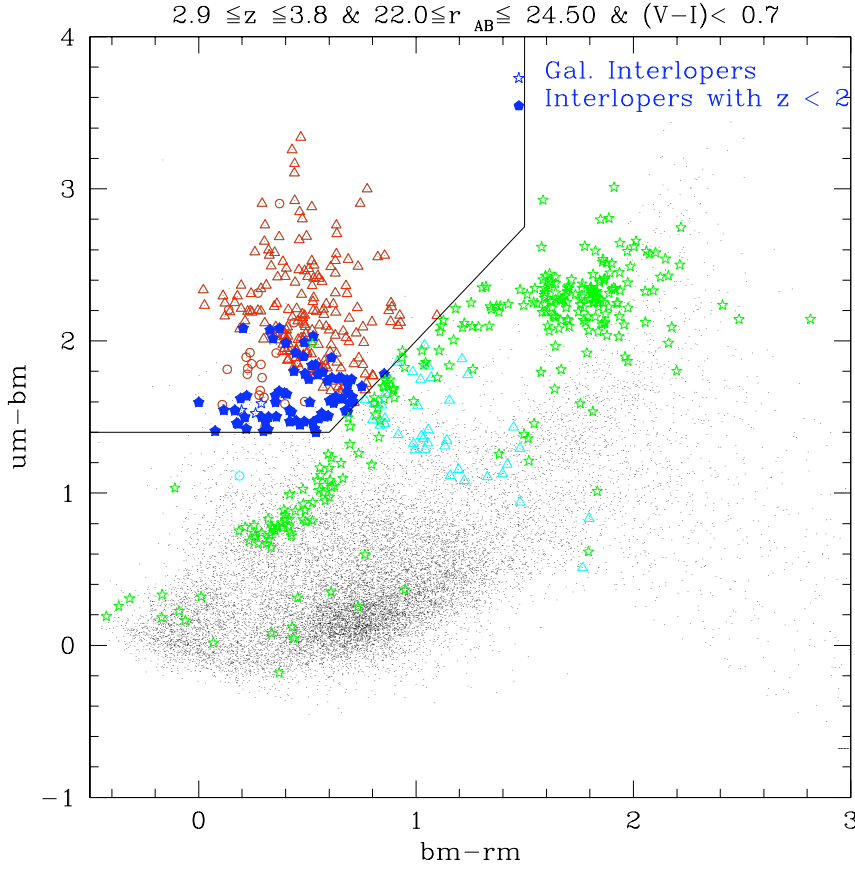


**Fig. 14.** a) Selection of U-dropout galaxies from color-color plots up to  $R_{AB} \leq 24.5$  (left panel) and  $R_{AB} \leq 25$  (right panel) with  $(V-I) \leq 0.8$  selection. The total area is  $0.0976 \text{ deg}^2$ . The simulated U-dropouts are in green open circles and triangles (upper-limit at  $1\sigma$ ). The selected ones in the box are in blue. The interlopers are shown in red hexagons ( $z \leq 2$ ) and red stars ( $z \leq 2.9$ ). b) Comparison with the fraction of observed objects

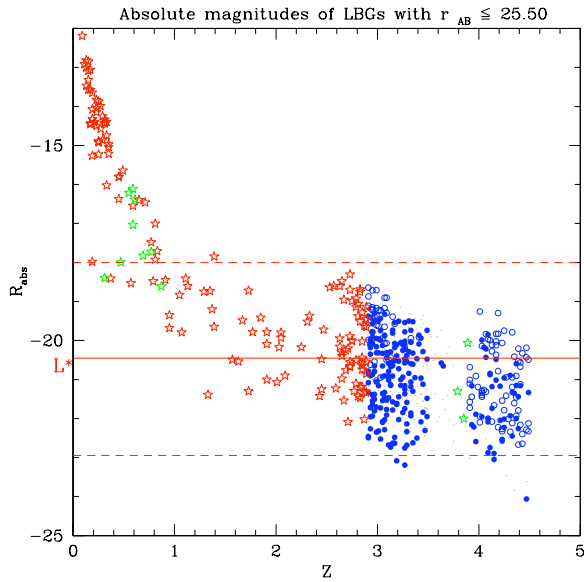


**Fig. 15.** Predicted absolute magnitude in R band for the selected Lyman break galaxy from the color-color diagrams. The candidates are shown with filled circles (for  $R \leq 25$ ) and open circles (for  $R \leq 25.5$ ). Interlopers for  $z \sim 3$  samples are shown as red stars and for  $z \sim 4$  sample as green stars. The solid line shows the absolute luminosity  $L_*$  from CNOC2 (Lin et al., 1999; for an EDS universe) and dotted lines the corresponding value for  $10 \times L_*$  (lower line) and  $0.1 \times L_*$  (upper line)